Progress In Electromagnetics Research, PIER 102, 351–366, 2010

THROUGH-WALL IMAGING: APPLICATION OF SUBSPACE-BASED OPTIMIZATION METHOD

T. Lu, K. Agarwal, Y. Zhong, and X. Chen

Department of Electrical and Computer Engineering
National University of Singapore
Singapore 117576, Singapore

Abstract—A model for two-dimensional layered medium is proposed for through-wall imaging problem. It is integrated with the subspace-based optimization method for reconstructing the relative permittivity profile in a fast and robust manner. Numerical results have shown that the concealed targets within walls can be reconstructed well using the proposed model even though full aperture of targets is not available due to the presence of walls. The model has also been employed for studying the effect of the presence of walls on imaging.

1. INTRODUCTION

Through-wall imaging aims to provide vision into otherwise obscured area by illumination of the area using electromagnetic waves. It has a variety of practical applications including fire rescue, emergency relief, and military operations. To our knowledge, such imaging problem has been approached in two ways: Some employed SAR processing methods and appropriately modified them in order to account for the presence of walls [1, 2]; others cast the imaging problem into an inverse scattering problem governed by wave equations [3–6]. In either case, it is well known that such inverse problem is nonlinear and ill-posed.

The focus of the present work is on the reconstruction using inverse scattering approach. Among the inverse scattering approaches, several numerical reconstruction methods have been applied for through-wall imaging. One such example is the contrast source inversion (CSI) [6–10]. Recently, subspace-based optimization method (SOM) has been proposed to solve inverse scattering problems [11–16]. SOM exhibits several advantages, such as robustness against noise and fast convergence. SOM divides the contrast source into two

Corresponding author: K. Agarwal (g0600069@nus.edu.sg).

parts: The deterministic part and the ambiguous part. Whereas the deterministic part is obtained by spectrum analysis, the ambiguous part is determined by optimization.

This paper extends the applicability of SOM to the through-wall imaging problem. In doing so, we notify several contributions to the inverse scattering problems in general and through-wall imaging problem in particular. One contribution of this paper is to present SOM as a fast solver for such an imaging problem. In contrast to CSI, which typically requires a few hundred iterations, SOM converges very fast owing to the spectrum analysis.

It is a well-known fact that the aperture plays a very important role in the inverse scattering problems. Even though most inverse scattering problems assume the availability of full aperture, often full aperture is not available and only a partial view of the imaging domain has to be employed. In such scenario, the quality of reconstruction often degrades significantly. Through the application of SOM in through-wall imaging, we demonstrate that SOM provides good reconstruction even when only partial aperture is available.

Even though the overall problem of through-wall imaging is complicated and challenging, numerical results show that the location, shape, and the constitutive parameters of the concealed targets are reconstructed well using SOM.

It is well known that the layered medium problem has wide applicability, not just in through-wall imaging, but also subsurface imaging, bio-medical imaging, etc. While many models resort to a homogeneous approximation of the scenario, the proposed model is applicable to a more realistic scenario in which layers are explicitly taken into account while imaging. Thus, the proposed method has wider applicability in the inverse problems and realistic imaging applications.

Another important contribution of the paper is to study the effect of the presence of walls on the quality of reconstruction. Generally, it is considered that multiple scattering effect enhances the quality of reconstruction. However, this opinion has not been conclusively proven to be true or otherwise [17]. Since the presence of walls or layers increases the amount of multiple scattering, it is interesting to see if multiple scattering indeed helps in improving the reconstruction. Since the effect of the presence of layers has been explicitly taken into account, it provides a direct framework for studying the effect of presence of walls on the imaging. We have presented a few examples for studying the effect of the presence of walls on the quality of reconstruction.

The outline of the paper is as follows. In Section 2, we describe

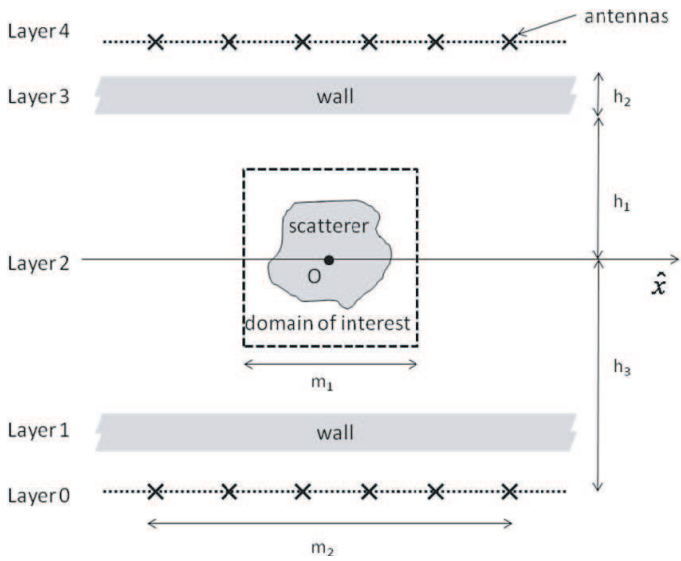

Figure 1. Schematic configuration of the layered medium model.

the problem and the setup. Section 3 presents the forward model for layered medium. SOM and the use of the forward model developed in Section 3 for reconstruction are presented in Section 4. Several numerical examples are presented in Section 5. The presented work is concluded in Section 6.

2. PROBLEM DESCRIPTION

The experimental setup and the problem are described in this section. In Figure 1, the square surrounded by dashed lines shows the domain of interest. The domain of interest is centered at the origin O with side length m_1. We discretize the domain of interest into M subunits, such that the electrical quantities on each unit can be considered constant. Two walls are positioned at a distance of h_1 from the x axis and the thickness of each wall is h_2 (shown in solid gray bars in Figure 1). Free space background is assumed between and beyond the walls. The complete setup, including the background medium, the walls and the scatterers, is non-magnetic. At a distance of h_3 from the origin, two linear arrays, each with a span of m_2, are set parallel to the walls. Each array has N_s number of antennas on it, thus $2N_s$ antennas in total. Antennas are symbolized by the crosses in Figure 1. The electric fields are along the z axis. Thus, the overall setting is transverse magnetic. Each antenna functions as a line source as well as a receiver.

While performing the measurements, one antenna acts as a source, while the scattered electric field is measured at all the antennas. This process is repeated for all the sources and a total number of $2N_s \times 2N_s$ measurements are collected. The measurements are stored in the matrix $\overline{\overline{E}}^{sca}$, where the (d, s)th element of $\overline{\overline{E}}^{sca}$ contains the scattered field corresponding to the dth detector and sth source. The problem of reconstruction involves the use of the measured scattered electric fields for determining the relative permittivity profile of the scatterers present in the domain which are concealed by the walls.

3. FORWARD MODEL

As shown in Figure 1, the presence of walls divides the region into five layers. Consequently, apart from direct propagations, we have to take into account both reflected and refracted signals coming from interactions with walls. The influence of walls is embedded into layered medium Green's Function [18–20].

3.1. Wave Propagation in Layered Medium

With reference to Figures 1 and 2, sources and receivers are located in the layers $l = 0$ and 4, whereas the domain of interest is located in the layer $l = 2$. Layers $l = 1$ and 3 are the layers of walls. The amplitude A_l ($l = 0$, 1, 2, 3, or 4) represents all wave components in layer l that have a propagating velocity component along the $\hat{y}$ direction, and B_l represents all wave components in layer l with a velocity component along the $(-\hat{y})$ direction. The wave number of the wave in layer l is given as follows:

$$k_l^2 = k_{ly}^2 + k_x^2. \tag{1}$$

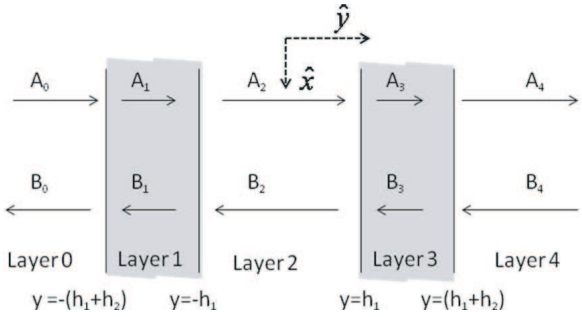

Figure 2. Wave propagation in layered model.

3.2. Layered Medium Green's Functions

3.2.1. Mapping from Sources to the Domain

The Green's function that maps the line current source located at $\vec{r}_s(x_s, y_s)$ (in the layer $l = 0$ or 4) to the electric field incident at a point $\vec{r}(x, y)$ in the domain (layer 2) is as follows:

$$G_{l2}(\vec{r}, \vec{r}_s) = \left(-\frac{\omega\mu_0}{4\pi}\right) \int_{-\infty}^{+\infty} \frac{e^{ik_x(x-x_s)}}{k_{ly}} \left(A_2 e^{i(k_{2y}y - k_{ly}y_s)} + B_2 e^{i(-k_{2y}y - k_{ly}y_s)}\right) dk_x, \quad (2)$$

where ω denotes the angular frequency of incidence, and μ_0 is the permeability of free space. It is worth noticing that A_2 and B_2 are the functions of integration variable k_x, the permittivity of the walls, and the geometric configuration of the walls. The exact expressions of A_2 and B_2, when the source is located in layer 0 or 4, can be obtained by matching the boundary conditions as done in [20]. For later convenience, we collect the above Green's function in a matrix $\overline{\overline{G}}_{inc} = [\ \overline{\overline{G}}_{02} \quad \overline{\overline{G}}_{42}\ ]$, where the (m, s)th element of $\overline{\overline{G}}_{02}$ is $G_{02}(\vec{r}_m, \vec{r}_s)$ and $\overline{\overline{G}}_{42}$ is $G_{42}(\vec{r}_m, \vec{r}_s)$, $\vec{r}_m$ represents the center point of the mth subunit, $m = 1$ to M, and $s = 1$ to N_s. Thus, the electric field incident at any subunit in the domain can be expressed as

$$\bar{E}^{inc} = \overline{\overline{G}}_{inc} \cdot \bar{I}^{src}, \quad (3)$$

where $\bar{I}^{src}$ contains the amplitude of currents at various sources.

3.2.2. Mapping from Current Induced in the Domain to Detectors

The Green's function that maps the induced current at a point $\vec{r}(x, y)$ in the domain (layer 2) to the scattered electric field received at a detector located at $\vec{r}_d(x_d, y_d)$ (in layer $l = 0$ or 4) is as follows:

$$G_{2l}(\vec{r}_d, \vec{r}) = \left(-\frac{\omega\mu_0}{4\pi}\right) \int_{-\infty}^{+\infty} \frac{e^{ik_x(x_d-x)}}{k_{2y}} \left(A_2 e^{i(k_{2y}y - k_{ly}y_d)} + B_2 e^{i(-k_{ly}y_d - k_{2y}y)}\right) dk_x, \quad (4)$$

Similar to the previous subsection, we collect the above Green's function into a matrix $\overline{\overline{G}}_{sca} = [\ \overline{\overline{G}}_{20}^{*} \quad \overline{\overline{G}}_{24}^{*}\ ]^{*}$, where the asterisk denotes the Hermitian operation, the (d, m)th element ($d = 1$ to N_s corresponds to the detectors) of $\overline{\overline{G}}_{20}$ is $G_{20}(\vec{r}_d, \vec{r}_m)$ and $\overline{\overline{G}}_{24}$ is $G_{24}(\vec{r}_d, \vec{r}_m)$.

It is notable that using the principle of reciprocity, for an antenna — subunit pair, Equations (2) and (4) are the same, and $\overline{\overline{G}}_{sca}$ is the transpose of $\overline{\overline{G}}_{inc}$. Thus, the scattered electric field due to the currents induced at various subunits in the domain can be expressed as:

$$\bar{E}^{sca} = \overline{\overline{G}}_{sca} \cdot \bar{I}^{d}, \tag{5}$$

where $\bar{I}^{d}$ contains the amplitude of induced currents at various subunits.

3.2.3. Mutual Multiple Scattering

It is well known that with the presence of extended scatterers, the electric fields from the sources are not the only electric fields observed at a point in the domain. The incident electric fields from primary sources induce secondary sources in the scatterers that have different electrical characteristics from the background, which contribute to the total electric fields observed at other points in the domain. This effect is called the multiple scattering effect. Among various ways of incorporating the mutual multiple scattering, we have used coupled dipole method [13, 21]. According to this model, the currents induced in a domain can be expressed as:

$$\bar{I}^{d} = \overline{\overline{\xi}} \cdot \left(\bar{E}^{inc} + \overline{\overline{G}}_{d} \cdot \bar{I}^{d} \right) = \overline{\overline{\xi}} \cdot \bar{E}^{tot}, \tag{6}$$

where $\overline{\overline{\xi}}$ is a diagonal matrix containing the electric polarization at the various subunits, $\bar{E}^{tot}$ represents the total electric field observed on the subunits, and $\overline{\overline{G}}_{d}$ maps the current induced at the subunits to the scattered electric field incident at the other subunits due to these induced currents. The mth diagonal element in $\overline{\overline{\xi}}$ is given by $\xi_m = -i\omega\varepsilon_0 a_m(\varepsilon_m - 1)$, where a_m and ε_m are the area and the relative permittivity of the mth subunit, respectively. The (m, n)th element in $\overline{\overline{G}}_{d}$ contains $G_d(\vec{r}_m, \vec{r}_n)$ which maps the induced current at a point $\vec{r}_n$ to the scattered field at the point $\vec{r}_m$, both $\vec{r}_n$ and $\vec{r}_m$ in the domain.

Evidently, $G_d(\vec{r}_m, \vec{r}_n)$ can be split into two parts: The mapping from currents in the domain to the subunits without considering the reflection from both of the walls, $G_{22}(\vec{r}_m, \vec{r}_n)$, and the mapping from currents in the domain to the subunits considering only the reflection from the walls, $G_{22,walls}(\vec{r}_m, \vec{r}_n)$. The expression for $G_{22}(\vec{r}_m, \vec{r}_n)$ is as follows:

$$G_{22}\left(\vec{r}_m, \vec{r}_n\right) = -\frac{\omega\mu_0}{4\pi} H_0^{(1)}\left(k_2 \left|\vec{r}_m - \vec{r}_n\right|\right), \tag{7}$$

The expression for $G_{22,walls}(\vec{r}_m, \vec{r}_n)$ is given as:

$$G_{22,walls}(\vec{r}_m, \vec{r}_n) = \left(-\frac{\omega\mu_0}{4\pi}\right) \int_{-\infty}^{+\infty} \frac{e^{ik_x(x_m - x_n)}}{k_{2y}} \left(A_2 e^{ik_{2y}(y_m - y_n)} + B_2 e^{ik_{2y}(-y_m - y_n)}\right) dk_x, \quad (8)$$

The exact expressions of A_2 and B_2, when the source is located in layer 2, can be obtained by matching the boundary conditions as done in [20]. Subsequently, $G_d(\vec{r}_m, \vec{r}_n)$ can be written as:

$$G_d(\vec{r}_m, \vec{r}_n) = G_{22}(\vec{r}_m, \vec{r}_n) + G_{22,walls}(\vec{r}_m, \vec{r}_n) \quad (9)$$

4. INVERSE SOLUTION: SOM

The Equations (5) and (6) together form the complete forward model. Equation (5) is called the field equation, while Equation (6) is called the state equation. In this section, we introduce the subspace based optimization method in the context of this formulation [11]. The singular value decomposition (SVD) of $\overline{\overline{G}}_{sca}$ can be represented as $\overline{\overline{G}}_{sca} = \overline{\overline{U}} \cdot \overline{\overline{S}} \cdot \overline{\overline{V}}^*$, where $\overline{\overline{U}}$ consists of the left singular vectors $\bar{u}_p$, $\overline{\overline{V}}$ consists of the right singular vectors $\bar{v}_p$, and $\overline{\overline{S}}$ is a diagonal matrix containing singular values σ_p. It is notable that the rank of $\overline{\overline{G}}_{sca}$ is much lesser that the number of subunits (due to lesser number of measurements) and the trailing values of σ_p are negligibly small, close to zero.

Because of this, the problem is under-determined and $\bar{I}^d$ cannot be retrieved correctly. SOM decomposes the space spanned by $\bar{I}^d$ into two subspaces, the signal subspace composed of the first L right singular vectors and the noise subspace composed of the remaining right singular vectors. The choice of the value of L is discussed in [13]. Due to this decomposition, the induced current $\bar{I}^d$ can be understood as composed of the deterministic part $\bar{I}^s$ and ambiguous part $\bar{I}^n$, corresponding to the signal and noise subspaces respectively. Accordingly, $\bar{I}^s$ can be uniquely determined analytically as $\bar{I}^s = \sum_{p=1}^{L} \sigma_p^{-1}(\bar{u}_p^* \cdot \bar{E}^{sca})\bar{v}_p$, and $\bar{I}^n$ has to be retrieved through optimization [11].

Let the ambiguous portion of the induced currents be $\bar{I}^n = \overline{\overline{V}}^n \cdot \bar{\alpha}^n$, where $\overline{\overline{V}}^n$ comprises of the right singular vectors $\bar{v}_p$ $(p > L)$, and $\bar{\alpha}^n$ contains the weights of vectors $\bar{v}_p$ $(p > L)$ in $\bar{I}^n$. The cost function,

which is a combination of the residues in the field equation and the state equation for all the incidences, is defined as:

$$\Delta = \sum_{s=1}^{2N_s} \left(\frac{\left\| \overline{\overline{G}}_{sca} \cdot \overline{\overline{V}}^{n} \cdot \bar{\alpha}_s^n + \overline{\overline{G}}_{sca} \cdot \bar{I}_s^d - \bar{E}_s^{sca} \right\|^2}{\left\| \bar{E}_s^{sca} \right\|^2} + \frac{\left\| \overline{\overline{A}} \cdot \bar{\alpha}_s^n - \bar{B}_s \right\|^2}{\left\| \bar{I}_s^d \right\|^2} \right), \quad (10)$$

where $\overline{\overline{A}} = (\overline{\overline{V}}^{n} - \overline{\overline{\xi}} \cdot \overline{\overline{G}}_d \cdot \overline{\overline{V}}^{n})$, $\bar{B}_s = \overline{\overline{\xi}} \cdot (\bar{E}_s^{inc} + \overline{\overline{G}}_d \cdot \bar{I}_s^d) - \bar{I}_s^d$, $\bar{\alpha}_s^n$ can be computed by applying least squares pseudoinverse on $\overline{\overline{A}} \cdot \bar{\alpha}_s^n = \bar{B}_s$, and the optimization variables ξ_m ($m = 1$ to M) are embedded in the cost function Δ through $\overline{\overline{\xi}}$. We use Levenberg-Marquardt (LM) optimization method to reconstruct the variables ξ_m ($m = 1$ to M).

The forward model developed in Section 3 gives the scattered field due to the scatterers in the domain only. All the Green's functions presented in Section 3 incorporate the effect of the walls and their combination using (5) and (6) gives the perturbation (scattered field) due to the scatterers directly. Thus, the SOM model does not need to consider the walls as the inhomogeneities and the matrix $\overline{\overline{\xi}}$ contains only the domain subunits.

Though the computation of Green's functions in the proposed model involves integration, which makes it computation intensive, the Green's functions need to be calculated only once for a setup and can be used for different scatterer profiles. Since the effect of the walls is taken into account in the Green's function through a complete analytical expression, no approximation is needed to account for the walls. In practice, for calculating the Green's functions, a finite interval is chosen instead of the infinite interval of integration. However, if the finite interval is sufficiently large, the error in the calculation of Green's function is small.

5. NUMERICAL EXAMPLES

We consider two numerical examples to demonstrate the efficacy of SOM in through-wall imaging. In both the examples, the basic setup is the same while the scatterer profile is different. With reference to Figure 1, the wall configuration is given by $h_1 = 1.2\,\text{m}$, $h_2 = 0.2\,\text{m}$, and the relative permittivity of both the walls is 3. The size of the domain is given by $m_1 = 1\,\text{m}$. The antenna configuration is given by $h_3 = 3\,\text{m}$, $m_2 = 6\,\text{m}$, and $N_s = 10$ (i.e., total 20 antennas). Due to the presence of the walls, the aperture available is inherently limited. The present antenna arrangement is such the antenna array on each side subtends an angle of 90° on the origin. The measurement setup is shown in Figure 3.

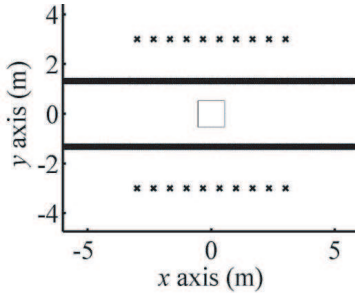

Figure 3. Measurement setup.

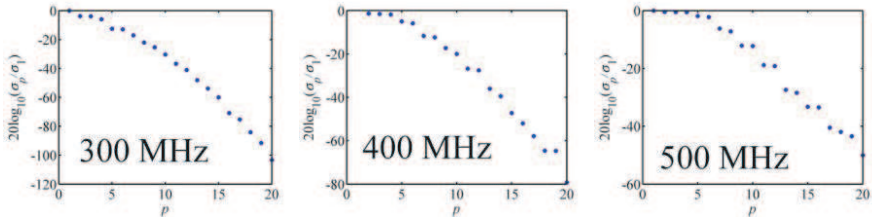

Figure 4. Plots of singular values of $\bar{\bar{G}}_{sca}$ for the three frequencies.

The domain is discretized into 25 equal subunits in each direction, such that $M = 625$. The measurements are performed for three different frequencies: 300 MHz, 400 MHz, and 500 MHz. The singular values of $\overline{\overline{G}}_{sca}$ for the three frequencies are plotted in Figure 4. The values of L chosen for the three frequencies are 6, 8, and 10 respectively.

In order to facilitate quantitative comparison, we define the reconstruction error as follows:

$$\text{error} = \frac{\sqrt{\sum_{\forall m} \left(\varepsilon_m^{act} - \varepsilon_m^{rec}\right)^2}}{\sqrt{\sum_{\forall m} \left(\varepsilon_m^{act}\right)^2}}, \tag{11}$$

where ε_m^{act} is the actual permittivity of the mth subunit while ε_m^{rec} is the reconstructed value of permittivity for the mth subunit.

5.1. Example 1

In the first example, the domain contains two square shaped scatterers with their centers at $(-0.25, 0)$ m and $(0.25, 0)$ m, and size 0.3 m each. The relative permittivities of the squares are 2 and 2.5,

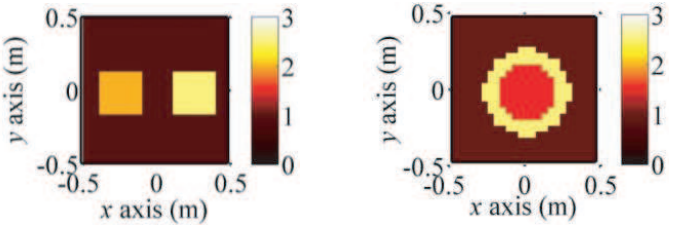

(a) Example 1: Two squares (b) Example 2: Ring and disk

Figure 5. Relative permittivity profile of the scatterers in the two examples. The color bar shows the relative permittivity.

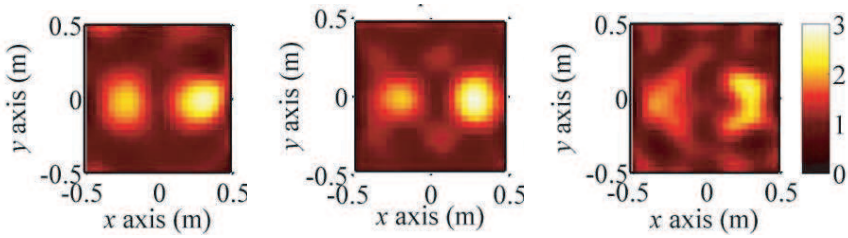

(a) 300 MHz (b) 400 MHz (c) 500 MHz

Figure 6. Reconstruction results for example 1 for the three frequencies considering initial guess of free space in the presence of 10% white Gaussian noise (after 30 iterations).

respectively. The relative permittivity profile is shown in Figure 5(a). The measurement data is corrupted with 10% additive white Gaussian noise. The details regarding the method of addition of noise can be found in [13].

The reconstruction results for the three frequencies after 30 iterations of optimization are shown in Figure 6. In this case, for all the three frequencies the initial value of ξ_m ($m = 1$ to M) is set to zero (i.e., free space). The errors in reconstruction for 300 MHz, 400 MHz, and 500 MHz are 0.192, 0.213, and 0.233 respectively. It can be seen that the two squares can be satisfactorily reconstructed for 300 MHz and 400 MHz, even though the permittivity of the walls is higher than both the squares. However, the reconstruction result is poor for higher frequencies.

In order to improve the reconstruction at higher frequencies, we use frequency hopping, where the relative permittivity reconstructed at 300 MHz is used as the initial guess for performing optimization on the measurement data of 400 MHz and the relative permittivity thus

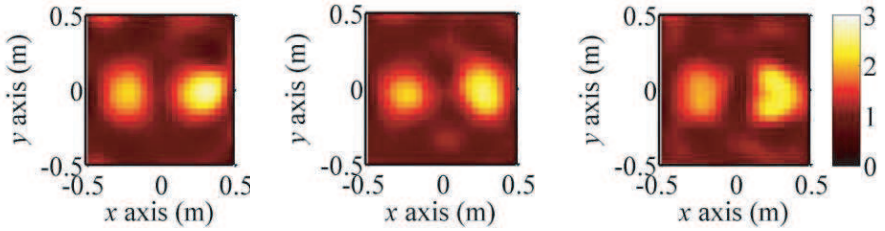

(a) 300 MHz (b) 400 MHz (c) 500 MHz

Figure 7. Reconstruction results for example 1 using frequency hopping in the presence of 10% white Gaussian noise (after 30, 4, and 3 iterations for (a), (b), (c) respectively).

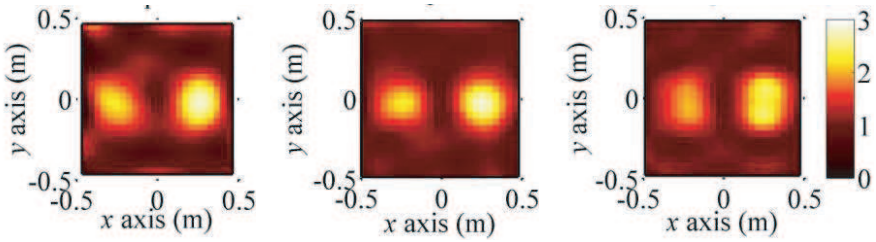

(a) 300 MHz (b) 400 MHz (c) 500 MHz

Figure 8. Reconstruction results for example 1 using frequency hopping in the presence of 7% white Gaussian noise.

reconstructed at 400 MHz is used as an initial guess for the optimization on the measurement data of 500 MHz. The optimization converges very fast for 400 MHz and 500 MHz. The frequency hopping results shown in Figure 7 are obtained after 30 iterations for 300 MHz, 4 iterations for 400 MHz and 3 iterations for 500 MHz. The respective errors in reconstruction are 0.192, 0.170, and 0.142. It is evident that frequency hopping improves the reconstruction significantly.

Figure 8 shows the reconstruction results for frequency hopping corresponding to 7% additive white Gaussian noise. The respective errors in reconstruction are 0.165, 0.147, and 0.116, which agree with the fact that the reconstruction results are better if the noise level is slightly less (7%).

5.2. Example 2

In the second example, we consider a combination of an annular ring and a circular disk. Both are centered at the origin. The disk has a

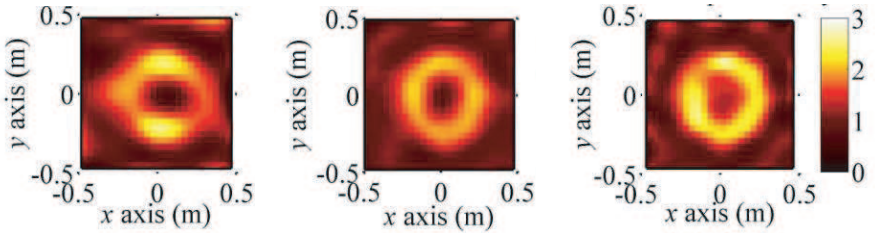

(a) 300 MHz (b) 400 MHz (c) 500 MHz

Figure 9. Reconstruction results for example 2 using frequency hopping in the presence of 10% noise.

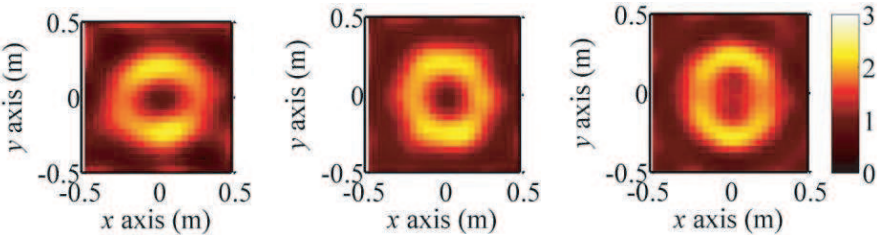

(a) 300 MHz (b) 400 MHz (c) 500 MHz

Figure 10. Reconstruction results for example 2 using frequency hopping in the presence of 7% noise.

radius of 0.2 m and relative permittivity 1.5, while the annular ring has inner radius of 0.2 m, outer radius of 0.3 m, and relative permittivity 2.5. The relative permittivity profile is shown in Figure 5(b). Since this example is more complicated than before, we show the reconstruction results obtained by frequency hopping only. Figures 9 and 10 show the reconstruction results for the measurement data corrupted by 10% and 7% noise respectively. The errors in reconstructions are 0.190 for Figure 9(c) and 0.145 for Figure 10(c). It is noticeable that the inner circle's relative permittivity is also reconstructed well using frequency hopping.

5.3. Effect of the Walls: Multiple Scattering

In this sub-section, we consider the effect of the presence of walls on the quality of reconstruction. For this purpose, we consider three scenarios:

1) Layer 1 and layer 3 have walls of relative permittivity 3 (as in previous examples).

2) Only layer 1 has a wall (of relative permittivity 3).
3) Both layers 1 and 3 have no walls.

We fix the measurement frequency as 300 MHz for comparing the three scenarios. For these three cases, we present the plots of singular values of $\overline{\overline{G}}_{sca}$ in Figure 11. It can be seen that the three cases do not have any significant difference in terms of the strengths of the singular values.

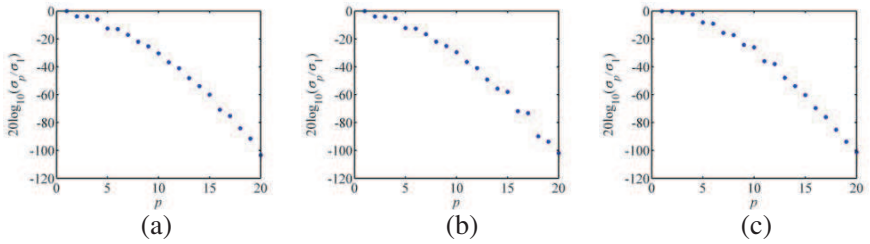

Figure 11. Plots of singular values of $\bar{\bar{G}}_{sca}$ for the three cases: two walls, one wall, and no wall. (a) Both walls are present, (b) wall in layer 1 is present, (c) no wall is present.

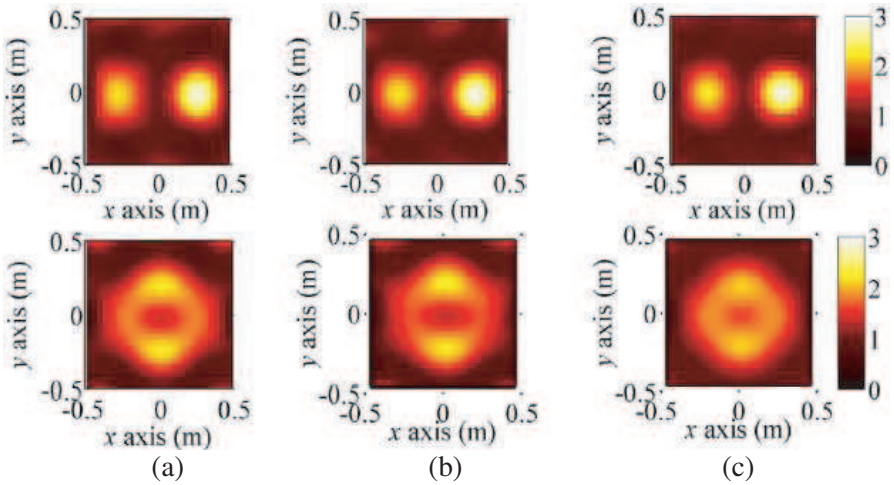

Figure 12. The reconstruction results of the two examples in the noise free scenario for the three cases (two walls, one wall, no wall). (a) Both walls are present, (b) wall in layer 1 is present, (c) no wall is present.

For a fair comparison of the quality of reconstruction, we consider that the measurement is noise-free for all the three cases. The reconstruction results for both the examples (in Figure 5) are shown in Figure 12. The optimization takes 9 or 10 iterations in each case to converge to the results shown. The error in reconstruction for example 1 is between 0.150 and 0.160 for all the three cases, while it is between 0.160 and 0.170 for the example 2 for all the three cases. Though it is difficult to compare the quality of the reconstruction, we can conclude that the multiple scattering effect does not necessarily enhance the quality of imaging. However, there is one noticeable difference in the three cases. When the walls are present (cases 1 and 2), the reconstruction pattern on the left and right sides seem elongated or broadened. This effect is more strongly visible for the second example, though present in both the examples. This can be explained by the presence of larger mutual coupling due to the presence of walls.

6. CONCLUSION

This paper applies the subspace-based optimization method for through-wall imaging. It uses an analytical model to account for the effect of walls such that the subspace-based optimization method can be applied in a straight forward manner. Hidden targets of different profiles are well reconstructed even in the presence of significant amount of noise and absence of full aperture for imaging. In all the examples presented, at most 30 iterations of optimization are sufficient. The use of frequency hopping provides good reconstruction results. Finally, the combination of the analytical model for layered medium and the subspace-based optimization method has been used to study the effect of the walls on the quality of reconstruction. It is shown that the presence of walls does not greatly affect the quality of reconstruction.

ACKNOWLEDGMENT

The authors thank the financial support of the US Department of the Air Force AOARD R&D Grant 094130.

REFERENCES

1. Dehmollaian, M., M. Thiel, and K. Sarabandi, "Through-the-wall imaging using differential SAR," *IEEE Trans. Geosci. Remote Sensing*, Vol. 47, No. 5, 1289–1296, May 2009.

2. Ertin, E. and R. L. Moses, "Through-the-wall SAR attributed scattering center feature estimation," *IEEE Trans. Geosci. Remote Sens.*, Vol. 47, No. 5, 1338–1348, May 2009.
3. Debes, C., M. G. Amin, and A. Zoubir, "Target detection in single- and multiple-view through-the-wall radar imaging," *IEEE Transactions on Geoscience and Remote Sensing*, Vol. 47, No. 5, 1349–1361, 2009.
4. Zheng, W., Z. Zhao, Z. P. Nie, and Q. H. Liu, "Evaluation of TRM in the complex through wall environment," *Progress In Electromagnetic Research*, PIER 90, 235–254, 2009.
5. Yoon, Y. and M. Amin, "High-resolution through-the-wall radar imaging using beamspace MUSIC," *IEEE Transactions on Antennas and Propagation*, Vol. 56, No. 6, 1763–1774, 2008.
6. Song, L. P., C. Yu, and Q. H. Liu, "Through-wall imaging (TWI) by radar: 2-D tomographic results and analyses," *IEEE Trans. Geosci. Remote Sens.*, Vol. 43, No. 12, 2793–2798, Dec. 2005.
7. Van Den Berg, P. M. and R. E. Kleinman, "A contrast source inversion method," *Inverse Problems*, Vol. 13, 1607–1620, 1997.
8. Abubakar, A. and P. M. van den Berg, "The contrast source inversion method for location and shape reconstructions," *Inverse Problems*, Vol. 18, No. 2, 495–510, Mar. 2002.
9. Van Den Berg, P. M. and A. Abubakar, "Contrast source inversion method: State of art," *Progress In Electromagnetics Research*, Vol. 34, 189–218, 2001.
10. Habashy, T. M., M. L. Oristaglio, and A. T. D. Hoop, "Simultaneous nonlinear reconstruction of two-dimensional permittivity and conductivity," *Radio Sci.*, Vol. 29, No. 4, 1101–1118, 1994.
11. Chen, X., "Application of signal-subspace and optimization methods in reconstructing extended scatterers," *J. Opt. Soc. Amer. A*, Vol. 26, No. 4, 1022–1026, 2009.
12. Zhong, Y. and X. Chen, "Twofold subspace-based optimization method for solving inverse scattering problems," *Inverse Problems*, Vol. 25, 085003, 2009.
13. Chen, X., "Subspace-based optimization method for solving inverse scattering problems," *IEEE Transactions on Geoscience and Remote Sensing*, Vol. 48, 42–49, 2010.
14. Pan, L., K. Agarwal, Y. Zhong, S. P. Yeo, and X. Chen, "Subspace-based optimization method for reconstructing extended scatterers: Transverse electric case," *Journal of the Optical Society of America A*, Vol. 26, 1932-7, 2009.
15. Agarwal, K., P. Li, and X. Chen, "Subspace-based optimization

method for reconstruction of two-dimensional complex anisotropic dielectric objects," *IEEE Trans. Microwave Theory and Technique*, Accepted, 2009.

16. Ye, X., X. Chen, Y. Zhong, and K. Agarwal, "Subspace-based optimization method for reconstructing perfectly electric conductors," *Progress In Electromagnetic Research*, PIER 100, 119–128, 2010.
17. Chen, X. and Y. Zhong, "Influence of multiple scattering on the resolution in inverse scattering," *Journal of the Optical Society of America A*, Vol. 27, 245–250, 2010.
18. Cui, T. J., W. C. Chew, X. X. Yin, and W. Hong, "Study of resolution and super resolution in electromagnetic imaging for half-space problems," *IEEE Trans. on Antennas and Propagation*, Vol. 52, 1398–1411, 2004.
19. Chew, W. C., *Waves and Fields in Inhomogeneous Media*, 2nd edition, IEEE Press, New York, 1995.
20. Kong, J. A., *Electromagnetic Wave Theory*, John Wiley & Sons, New York, 1990.
21. Lakhtakia, A., "Strong and weak forms of the method of moments and the coupled dipole method for scattering of time-harmonic electromagnetic fields," *International Journal of Modern Physics C*, Vol. 3, 583–603, 1992.